Acta Astronautica 203 (2023) 577–591

Contents lists available at ScienceDirect

Acta Astronautica

journal homepage: www.elsevier.com/locate/actaastro

Robust stability and mission performance of a CubeSat orbiting the Didymos binary asteroid system

Iosto Fodde *, Jinglang Feng, Annalisa Riccardi, Massimiliano Vasile

Department of Mechanical and Aerospace Engineering, University of Strathclyde, 75 Montrose Street, Glasgow, G1 1XJ, United Kingdom

ARTICLE INFO

Keywords:
Didymos system
Orbital stability
Uncertainty analysis
Mission design

ABSTRACT

The dynamics of a CubeSat orbiting a binary asteroid system can be quite complex due to the irregular gravitational fields of the two bodies and the significant effect of the Solar radiation pressure. Furthermore, the large distance to Earth and the small size of the bodies result in difficulties in the observational process and brings about significant uncertainties in the modelling of the dynamics. In this work, the robust stability and mission performance of orbits in a binary asteroid system under uncertainty are studied with three novel dynamics indicators. The uncertainty in the dynamics is propagated with a polynomial algebra over the space of Taylor polynomials and the indicators are derived from the coefficients of the propagated polynomials. These indicators are found to show accurately the regions of robust stability and bounded motion around Didymos. In addition to the indicators, the observability of Dimorphos for different initial conditions is also studied. The analysis shows a correspondence between the level of robust stability and the size of the observability bounds, albeit the geometry of certain orbits limits the potential maximum observability.

1. Introduction

The Asteroid Impact and Deflection Assessment (AIDA) is a collaborative mission to test the effectiveness of a kinetic impactor to change the trajectory of the binary asteroid system (65803) Didymos consisting of the primary body Didymos and smaller moon Dimorphos. ESA's contribution to AIDA, the Hera mission, will visit the asteroid in late 2026 after NASA's DART spacecraft impacted Dimorphos in September 2022. Hera aims to characterise the physical properties of the binary system and investigate the consequence of the impact in more detail [1]. Besides the larger Hera mother spacecraft, two CubeSats (called Milani [2] and Juventas [3]) will be released into orbits around the system. The Hera spacecraft plans to follow hyperbolic arcs around the system, while the CubeSats will use the natural dynamics of the system to orbit more closely to the bodies (for Milani, this only holds for the final phase of the mission as mainly it will also use hyperbolic arcs). The dynamical environment around a binary asteroid system is characterised by a weak and irregular gravity field from both bodies, and a significant influence from the solar radiation pressure (SRP) effect [4]. This makes the orbit design process for the CubeSats more challenging.

Due to the complex dynamics around a binary asteroid system, it is important to find specific orbits that remain stable for longer periods of time, as this can significantly reduce the amount of station-keeping maneuvers and reduce the risk of an impact or escape from the system in case of failures. In [5] the stability of orbits close to the bodies were investigated by analysing the lifetime of a large range of different orbits using numerical investigations. It was shown that the SRP has a large effect on the lifetime of certain orbits. Further search for stable orbits around Didymos in [6] showed that some orbits that were found to be nominally stable, e.g. Lagrange point orbits, are not stable anymore under larger variations in the state vector by looking at the percentage of orbits that survive through a Monte Carlo analysis. Another method of trajectory analysis was performed in [7], where the Lagrangian Coherent structures (LCS) were identified for an asynchronous binary asteroid system, which are the non-autonomous counterparts to invariant manifolds. More recently, [8] analysed the different dynamical regimes around Didymos and determined favourable trajectories by employing a waypoint strategy where the orbit control system is used more frequently.

In the previously mentioned studies, only the nominal system was investigated, or only after the nominal design was performed were the uncertainties included. This is more time intensive, and for larger uncertainties it can affect which orbits are determined to be stable [6]. Due to the difficulty of accurately modelling asteroids from remote observations, uncertainties in the model variables can be larger compared to other missions [9]. The main sources of uncertainties in small body exploration are discussed in [10]. A technique based on the expansion

* Corresponding author.
E-mail address: iosto.fodde@strath.ac.uk (I. Fodde).

https://doi.org/10.1016/j.actaastro.2022.12.021
Received 31 March 2022; Received in revised form 28 October 2022; Accepted 18 December 2022
Available online 20 December 2022

of the uncertain state in terms of Taylor polynomials was used to determine the effect of uncertainties on the stability of a spacecraft around an asteroid in [11]. This technique was able to analyse the effects of non-spherical gravity uncertainties, and found that the motion is sensitive to variations in the C_{22} term. Further analyses on the effect of uncertain SRP and asteroid mass was performed in [12,13]. These studies highlighted the importance of accounting for the effect of uncertainties on the stability of orbits around an asteroid.

Based on the previously mentioned studies, novel indicators were proposed by the authors in [14] to analyse the effect of uncertainties in dynamical systems. This work further builds upon this by analysing a dynamical system that more closely represents that experienced by the Hera CubeSats, and includes several other uncertainties (i.e. the initial state, Didymos shape parameters, and the SRP force) which allow for the determination of stable orbits that are also robust against these dynamical uncertainties. Additionally, the indicators are adapted to allow for the use of other state representations. Furthermore, the paper presents an analysis of the observability of Dimorphos for a range of possible orbits. This second objective, combined with the robust stability of the orbit, provides a measure of the overall mission performance.

The paper is structured as follows. First, in Section 2 the dynamical models used for the orbital motion of a spacecraft in the Didymos binary system are discussed. Afterwards the robust stability indicators are introduced in Section 3. Additionally, the observability analysis to provide an overall mission performance is discussed in Section 4. The final results will be presented in Section 5, and finally a conclusion and recommendations for possible future work is given in Section 6.

2. Dynamics in the Didymos system

The system studied for this work is the Didymos binary system consisting of the main body called Didymos (in other works also known as Didymain) and the secondary body Dimorphos (also known as Didymoon). A summary of the results of various observation campaigns to describe the physical models of the system can be found in [15], and is summarised here in Table 1.

The equations of motion of the CubeSat are described in a quasi-inertial Didymos equatorial reference frame (see Fig. 1). This means that the heliocentric motion of the Didymos system is not taken into account, as the time frames of the simulations discussed here are significantly shorter than the dynamical timescales of the motion of the system around the Sun. It is also assumed that the motion of Dimorphos around Didymos is described by a Keplerian orbit (with orbital parameters shown in Table 1). The x–y plane of the reference frame is defined to be in the binary's orbital plane, where the x-axis points in the direction of the Sun. The z-axis is parallel to the binary orbit normal. The rotational motion of both bodies is described by a uniform rotation around the reference frame's z-axis, and coincides with the inertial frame at time $t = 0$. Didymos rotates at a speed of 0.0442 deg/s, whereas Dimorphos is tidally locked with the primary and thus rotates at the same speed as the mean motion of its orbit around the primary. As the obliquity of the binary orbit is around 175 degrees with respect to the heliocentric orbit, the reference frame is flipped with respect to the $J2000$ frame, and the Sun is located 5 degrees above the Dimorphos orbit plane and thus 5 degrees above the x-axis of the quasi-inertial reference frame.

The equations of motion in the quasi-inertial frame I can be described as follows:

$$\boldsymbol{F}^I_{tot} = \boldsymbol{F}^I_{g,prim} + \boldsymbol{F}^I_{g,sec} + \boldsymbol{F}^I_{SRP} + \boldsymbol{F}^I_{g,Sun}, \tag{1}$$

where the specific forces of influence are the primary's gravity $\boldsymbol{F}^I_{g,prim}$, the secondary's gravity $\boldsymbol{F}^I_{g,sec}$, the SRP $\boldsymbol{F}^I_{SRP}$, and the gravity of the Sun $\boldsymbol{F}^I_{g,Sun}$.

For grid 2, the effect of e on the terminator orbits (see $i = 90°$ from Fig. 3) is investigated. The results are shown in Fig. 5. The eccentricity

Table 1
Physical parameters of the Didymos system, taken from [15].

System mass	$5.28\ (\pm\ 0.54) \cdot 10^{11}$ kg
Mass ratio	0.0093 ± 0.0013
Heliocentric eccentricity	$0.38\ \pm 7.7 \cdot 10^{-9}$
Heliocentric semimajor axis	1.64 AU ± 9.8e−9 AU
Heliocentric inclination	3.41 +/−2.4e−6 deg
Binary Orbit Obliquity	175 +/−9 deg
Primary	
Diameter	780 m ± 3 m
Rotational Period	2.26 h ± 0.0001 h
Ellipsoid semi-axes (a, b, c)	399, 392, 380 m
Secondary	
Diameter	164 m ± 18 m
Ellipsoid semi-axes (a, b, c)	103, 79, 66 km
Binary eccentricity	0.03 (upper limit)
Binary semimajor axis	1.19 km
Binary inclination	0.0 deg

can be seen to have a significant effect on the robust stability of an orbit. For higher semi-major axes, the eccentricity can be increased and the orbit remains relatively stable. While for low semi-major axes, small initial eccentricities can already lead to unstable orbits. Small values of e result in close approaches to the asteroid system in the case of low a, which results in destabilising effects due to the higher gravitational acceleration.

A set of sample trajectories from a similar Monte Carlo analysis as before are also plotted in Figs. 6(a) and 6(b). From these figures it seems as if trajectories from E are more stable then expected compared to F. However, from the evolution of the distance from the centre of Didymos and the velocity, seen in Fig. 7, it can be seen that the amplitude for both variables are decreasing over time for F. Whereas for E these are slightly increasing over time.

Here, a spherical harmonics model of Didymos is considered to calculate the force due to its non-spherical shape. The potential for the spherical harmonics model is given by [16]:

$$U(r,\delta,\lambda) = \frac{\mu}{r}\sum_{l=0}^{\infty}\sum_{m=0}^{l}\left(\frac{r_0}{r}\right)^l \quad P_{lm}(\sin\delta)[C_{lm}\cos m\lambda + S_{lm}\sin m\lambda] \tag{2}$$

where r is the radial distance from the center of the body, δ is the latitude, λ is the longitude, μ is the gravitational coefficient of the body, r_0 is a normalised radius which is often taken as the mean or maximum radial size of the body, P_{lm} are the Associated Legendre Functions (their expressions can be found in [4]), and C_{lm} and S_{lm} are the Stokes coefficients which represent the mass distribution of the body. The Stokes coefficients for Didymos are calculated based on the measured ellipsoidal shape parameters of Didymos, which are shown in Table 1, using the following equations [17]:

$$C_{20} = \frac{1}{5R^2}(c^2 - \frac{1}{2}(a^2+b^2)) = -0.016 \tag{3}$$

$$C_{22} = \frac{1}{20R^2}(a^2 - b^2) = 1.82e-2 \tag{4}$$

$$C_{40} = \frac{15}{7}(C_{20}^2 + 2C_{22}^2) = 5.5e-3 \tag{5}$$

$$C_{42} = \frac{5}{7}C_{20}C_{22} = -2.06e-5 \tag{6}$$

$$C_{44} = \frac{5}{28}C_{22}^2 = 5.91e-7 \tag{7}$$

For the main purpose of trajectory design, the spherical harmonics terms up to and including the fourth order need to be considered [18]. In the case of Didymos, the C_{20} and C_{22} terms are at least one order of magnitude larger than the higher order terms of the gravity field. As a large uncertainty of about 10 percent is considered in these second order coefficients, the higher order terms will have a significantly lower impact on the gravitational acceleration compared to the effect of the large uncertainties in C_{20} and C_{22}. Therefore, the spherical

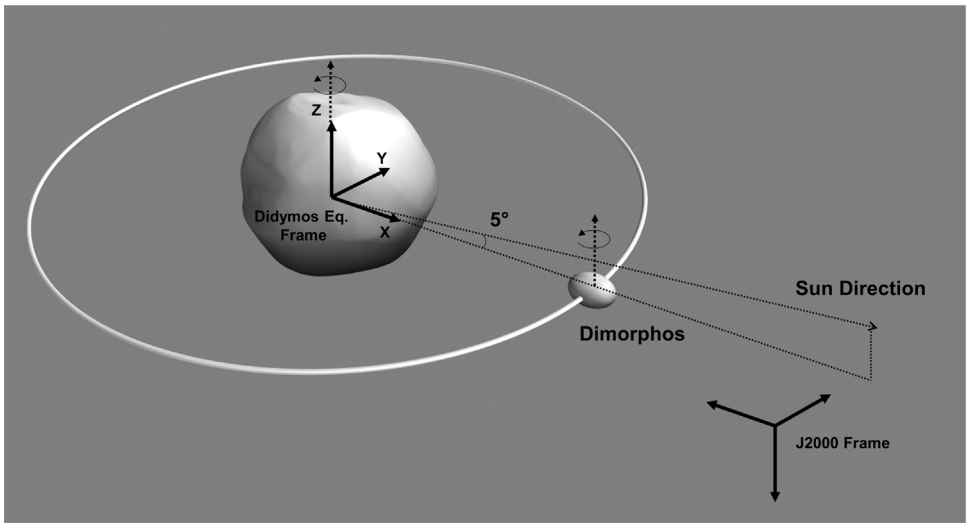

Fig. 1. The quasi-inertial Didymos equatorial reference frame and its orientation with respect to the J2000 ecliptic reference frame and the difference between Dimorphos' orbit and the Sun direction.

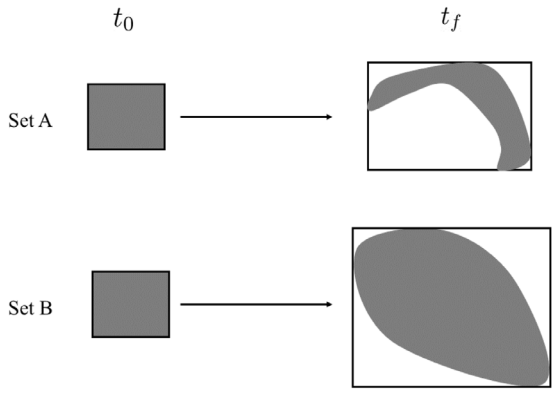

Fig. 2. Diagram showing two sets being propagated. The grey shaded area is where the actual trajectories are located and the black square represents the range of the set. Set A represent the propagation through more non-linear dynamics while set B has larger variance but is less non-linear.

harmonics acceleration is truncated at the second order and degree. Similarly, higher fidelity models based on the current polyhedron shape of Didymos (e.g. see [19]) would increase the accuracy of the calculated trajectories for the deterministic case, but for the uncertain case the accuracy improvement is less significant due to the uncertainties in the physical parameters considered for these models.

There are several methods to calculate the acceleration from Eq. (2). In this work, the representation of the spherical harmonics acceleration of [20] is used, where a transformation from the body frame to the inertial frame is needed. As the rotation axis of the primary is aligned with the z-axis of the inertial frame, only a rotation matrix around the z-axis is needed.

As the orbits considered are at a minimum distance of 2 km from the Didymos centre, the secondary is considered to have a point mass gravity field, as was shown to be sufficiently accurate for these dynamical regimes in [8]. The gravitation of the Sun is assumed to be described by a point mass as well, due to the large distance between the asteroids and the Sun.

For the SRP acceleration, a cannonball radiation pressure model is used. The acceleration for this model is given by the following formula [16]:

$$a_{SRP} = -(1+\kappa_s)\frac{P_0}{B}\cdot\frac{\boldsymbol{r}-\boldsymbol{r}_\odot}{|\boldsymbol{r}-\boldsymbol{r}_\odot|^3} \tag{8}$$

where κ_s is the albedo of the spacecraft, P_0 is the solar constant, B is the mass-to-area ratio of the spacecraft, $\boldsymbol{r}$ is the vector between Didymos and the spacecraft, and $\boldsymbol{r}_\odot$ is the vector between Didymos and the Sun. As was discussed before, the relative position of Didymos with respect to the Sun remains constant, and is located at a distance of 1.831 AU (The distance on July 2027, which is during the operational phase of the two CubeSats [21]). In this SRP model the specific difference in reference areas between the different sides of the CubeSat are not taken into account, as the uncertainties in the reference area considered in this work include these differences. The analysis of the effect of the (uncertain) attitude on the SRP force, similar to [22], is left for future work. The nominal value for the mass-to-area ratio of the CubeSat is taken as 25.86 $\mathrm{kg/m^2}$ (The mass-to-area ratio of Juventas [3]).

3. Robust stability

One class of techniques used for the analysis of stability in non-linear systems are dynamics indicators, such as the Fast Lyapunov Indicator [23] or the Finite Time Lyapunov Exponent [24]. These indicators measure the divergence of trajectories starting from nearby initial conditions. In the case that the dynamical parameters are only known with a high degree of uncertainty, these indicators would need to be recalculated for a sufficiently large amount of different realisations of these uncertain variables. This can be computationally expensive, especially when the dimensionality of the uncertain space becomes large.

Previously in [14], the authors introduced novel indicators that are able to capture the effect of these uncertain parameters as well. There, only the effect of the uncertain parameters were investigated. In this work, the sensitivity of the motion to both variations in the initial conditions and in model parameters is investigated using these indicators. This measure of sensitivity quantifies the robust stability of the motion.

We start by proposing a definition of robust stability. Then, a short overview of the Generalised Intrusive Polynomial Algebra (GIPA) technique, which is used to propagate uncertainty and from which the indicators are derived, is given in Section 3.1. Finally, the indicators used in this work to measure the robust stability are introduced in Sections 3.2 and 3.3.

Consider a set of initial states at time t_0 given by Ω_{x_0}. The set Ω_{x_0} represents all possible values of the state vector at time t_0 given the uncertainties in both the state $\boldsymbol{x}_0 = \boldsymbol{x}(t_0)$ and model parameters $\boldsymbol{\beta}$, which are combined into the uncertainty vector $\boldsymbol{\xi} = [\boldsymbol{x}_0, \boldsymbol{\beta}]$. As this

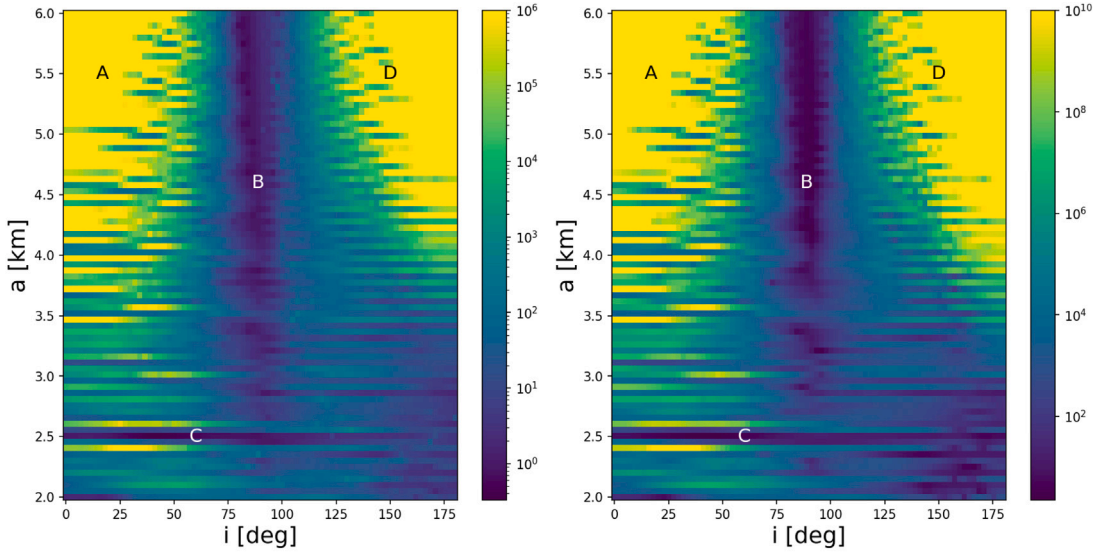

(a) η_{n+1}. (b) η_{σ}.

Fig. 3. The uncertain dynamics indicators for grid 1. The colourmaps represent the value of the respective indicator, thus the amount of variance and non-linearity. The letters indicate the set of sample orbits that are used to verify this grid, which are shown in Fig. 4.

set is propagated through the dynamical system, the set at any given future time is given by $\Omega_{\boldsymbol{x}_t}(\boldsymbol{\xi})$, which represents all possible values for the state at time t from realisations of $\boldsymbol{\xi}$ at time t_0. This can be defined formally as follows:

$$\Omega_{\boldsymbol{x}_t} = \{\boldsymbol{x}(t,\boldsymbol{\xi}) \mid \forall\, \boldsymbol{\xi} \in \Omega_{\boldsymbol{\xi}}\}, \tag{9}$$

where $\Omega_{\boldsymbol{\xi}}$ is a bounded uncertainty set and the states are propagated through the dynamical system $\boldsymbol{f}(\boldsymbol{x},\boldsymbol{\beta},t)$ as follows:

$$\boldsymbol{x}_t = \boldsymbol{x}(t) = \boldsymbol{x}_0 + \int_{t_0}^{t} \boldsymbol{f}(\boldsymbol{x},\boldsymbol{\beta},\tau)d\tau. \tag{10}$$

The variation of the volume of the set and its shape over time are a measure of the evolution of an ensemble of trajectories induced by multiple realisations of $\boldsymbol{\xi}$. If the trajectories are moving apart over time one would expect an increase in the volume of the set. On the other hand the set can stretch in one particular direction without increasing its volume. If the trajectories in the ensemble grow apart, whether increasing the volume of the set or just by stretching it in some directions, we call the process diffusive. The degree to which the trajectories in the ensemble grow apart is a function of the level of uncertainty and of the dynamics governing the evolution of each trajectory.

We can now provide a definition of robust stability.

Definition 3.1 (*Robust Stability*)**.** Given the uncertainty set $\Omega_{\boldsymbol{\xi}}$, the initial bounded set $\Omega_{\boldsymbol{x}_0}$ and propagated states (10), consider a restriction $\Omega_{\boldsymbol{y}_t}$ of $\Omega_{\boldsymbol{x}_t}$ to the subspace defined by only some of the components $\boldsymbol{y}_t$ of $\boldsymbol{x}_t$. A robust stable motion is such that for every realisation of $\boldsymbol{\xi} \in \Omega_{\boldsymbol{\xi}}$ every restriction $\Omega_{\boldsymbol{y}_t}$ is such that $\int_{\Omega_{\boldsymbol{y}_t}} d\boldsymbol{y}_t < \varepsilon_y$, $\forall t > 0$. In other words the motion remains bounded over time in all directions.

Following the definition of diffusion of an ensemble of trajectories, this means that if the diffusion remains low when parametric uncertainties are also considered, the orbit is defined to be robust stable. A robust stable orbit around an asteroid thus shows that the spacecraft will be stable, even if the true environment is different from the nominal dynamical model. Comparing the measure of robust stability between different initial conditions allows for the comparison of different regions in phase space against each other to determine regions of less sensitive motion.

In the following we will develop scalar indicators that capture the evolution of $\Omega_{\boldsymbol{x}_t}$ and will show how the value of these indicators gives an indication of the level of robust stability. The indicators will be derived from the propagation of the uncertainties through the dynamics. In this work, the uncertainty propagation is performed using the Generalised Intrusive Polynomial Algebra (GIPA) technique proposed in [25]. A brief overview of GIPA is given in Section 3.1.

3.1. Generalised intrusive polynomial algebra

To obtain an exact representation of the set $\Omega_{\boldsymbol{x}_t}$, an infinite number of samples from $\Omega_{\boldsymbol{\xi}}$ would need to be propagated. Thus, it is desirable to obtain an approximation of $\Omega_{\boldsymbol{x}_t}$. A generally applied approach for generating an analytical function to describe this set is a polynomial approximation, given by:

$$\tilde{\Omega}_{\boldsymbol{x}_t}(\boldsymbol{\xi}) = P_{n,d}(\boldsymbol{\xi}) = \sum_{i=1}^{\mathcal{N}} c_i(t)\alpha_i(\boldsymbol{\xi}), \tag{11}$$

where $\alpha_i(\boldsymbol{\xi})$ are a set of multivariate polynomial basis functions, $c_i(t_f)$ are the corresponding coefficients, and $\mathcal{N} = \binom{n+d}{d}$ is the number of terms of the polynomial, where n is the degree of the polynomial and d is the number of variables.

The GIPA method tries to obtain this final approximation by first using the α basis to approximate the initial set, and then taking the basis α and transforming it to a monomial basis, given by ϕ. A set of elementary operations, corresponding to the floating point operations $\oplus \in \{+,-,\cdot,/\}$, between the different polynomials in this basis is then constructed. With this setup only one set of operations needs to be defined for the monomial space, together with a transformation from the desired basis to the monomial basis. Then, for any operation between two functions f_a and f_b, the corresponding operations for their polynomial approximations, F_A and F_B, is given as follows:

$$f_a \oplus f_b \sim F_A \otimes F_B. \tag{12}$$

The polynomial space $\mathcal{P}_{n,d}(\alpha)$ and the operations on that space together form an algebra $(\mathcal{P}_{n,d}(\alpha), \otimes)$ of size $\mathcal{N}$, for which any polynomial part of this algebra is completely defined by its coefficients $c = \{c_{\boldsymbol{i}} : |\boldsymbol{i}| < n\}$. The specific ordering and definition of the indexing vector $\boldsymbol{i}$ can be found in [26].

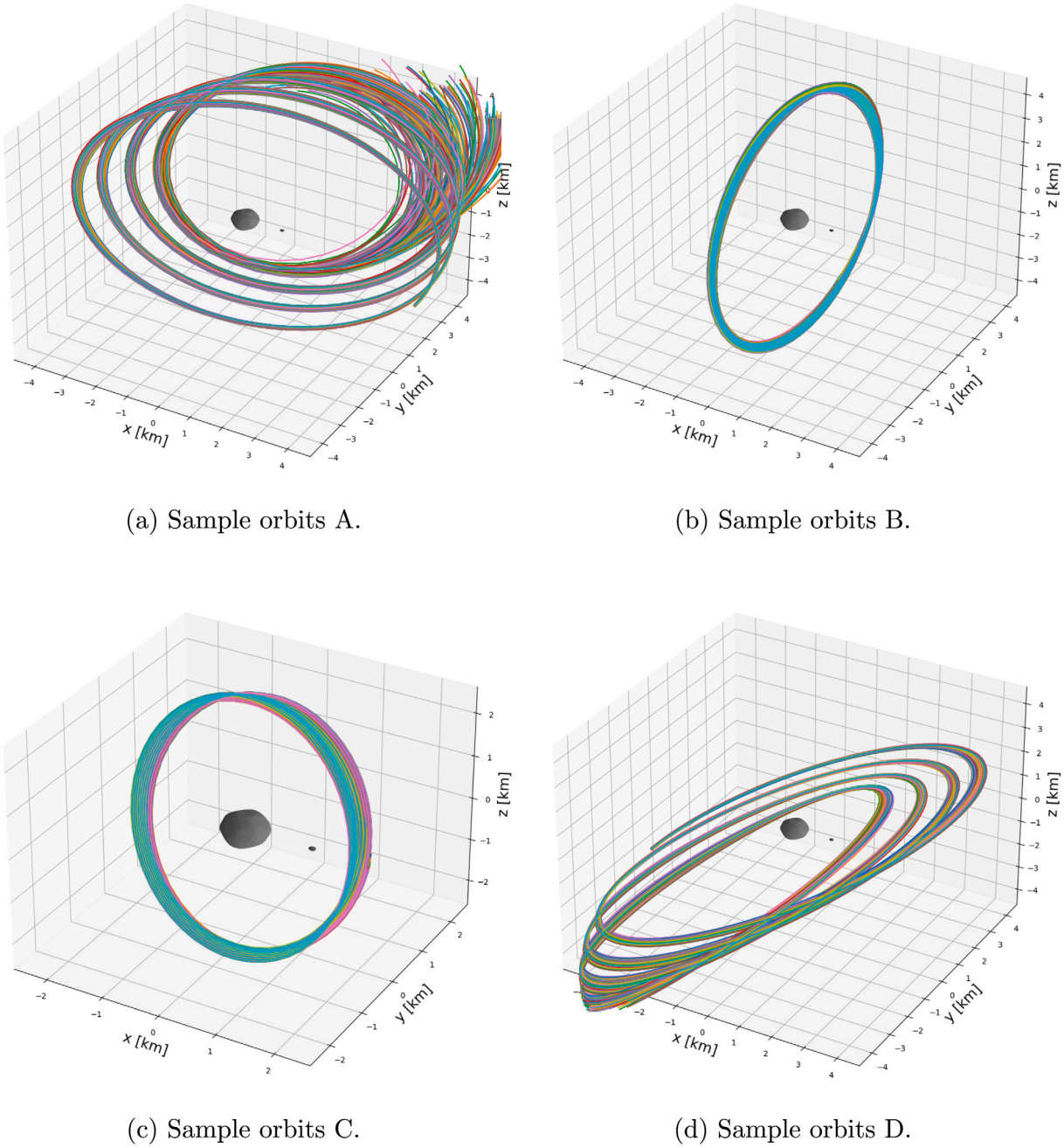

(a) Sample orbits A.

(b) Sample orbits B.

(c) Sample orbits C.

(d) Sample orbits D.

Fig. 4. Sample trajectories from the uncertain dynamics indicator maps propagated until $t_f = 8$ periods.

Next to the elementary operations, the algebra also needs to be able to implement a set of elementary functions $h(y)$, e.g. $\{1/y, \sin(y), \exp(y), \log(y), \text{etc.}\}$. For this, the composition operator is used as follows:

$$h(\boldsymbol{f}(\boldsymbol{x})) \sim H(y) \circ F(\boldsymbol{x}). \tag{13}$$

where $H(y)$ is the univariate polynomial approximation of $h(y)$ and $f(\boldsymbol{x})$ a multivariate function with $F(\boldsymbol{x})$ its polynomial approximation. In this case the composition operator is defined as:

$$\circ : \mathcal{P}_{n,1}(\phi) \times \mathcal{P}_{n,d}(\phi) \to \mathcal{P}_{n,d}(\phi). \tag{14}$$

With each polynomial basis, the polynomial approximation of the functions $H(y) \sim h(y)$ are performed differently. For example, for a Taylor polynomial basis these functions are approximated using a truncated Maclaurin series, whereas for a Chebyshev basis these functions are approximated using an order 100 Chebyshev interpolation. However, it was shown in [25] that for a Chebyshev basis this can lead to an overestimation of the bounds due to the fact that for these interpolations an estimate of the range of the polynomial is needed, for which the algorithm used leads to inaccuracies.

A comparison between a Chebyshev and a Taylor basis for uncertainty propagation in a binary asteroid system has been performed in [27]. As the uncertainty set can grow quickly in the case considered here, a Chebyshev basis would allow for better accuracy as it is more accurate for larger sets. However, due to the overestimation of the range with a Chebyshev basis, there is a large chance that the range of the expansion intersects with one of the bodies. Since the full range is taken into account for estimating the elementary functions, the Chebyshev basis expansion can cause possible divergences and singularities. For the Taylor basis this is less of a problem as the central point is used. Therefore, a Taylor basis is used for the rest of this work to avoid the numerical issues encountered when using a Chebyshev basis.

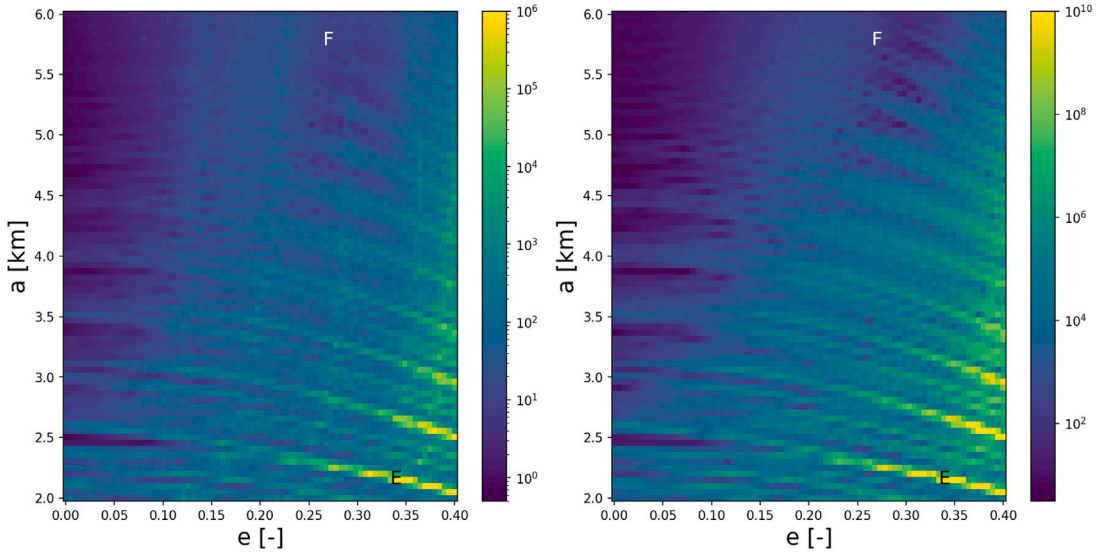

(a) η_{n+1}. (b) η_{σ}.

Fig. 5. The uncertain dynamics indicators for grid 2. The colourmaps represent the value of the respective indicator, thus the amount of variance and non-linearity.

Consider now the initial value problem given as follows:

$$\begin{cases} \dot{\boldsymbol{x}} = \boldsymbol{f}(\boldsymbol{x}, \boldsymbol{\beta}, t) \\ \boldsymbol{x}(t_0) = \boldsymbol{x}_0 \end{cases} . \tag{15}$$

The set of final values $\Omega_{\boldsymbol{x}_f}$ that result from the set of all possible values for $\boldsymbol{x}_0$ and $\boldsymbol{\beta}$ can now be found by representing these variables as members of the polynomial algebra ($\mathcal{P}_{n,d}(\alpha)$, $\otimes$), and using any numerical integrator algorithm (e.g. Runge–Kutta 4) to propagate them to the desired time t. The functions and operations in both the numerical integrator and dynamical models (e.g. spherical harmonics gravity) are swapped with their counterparts from the algebra to be able to use them with $\boldsymbol{X}$ and $\boldsymbol{B}$, which are the representations of $\boldsymbol{x}$ and $\boldsymbol{\beta}$ in the polynomial algebra.

Due to several features in modern coding languages, e.g. operator overloading and templates, this can be easily done without changing the underlying numerical implementations of the dynamics. The Stratchlyde Mechanical and Aerospace Research Toolbox for Uncertainty Quantification (SMART-UQ) [28] is used for the implementation of the GIPA method in a computer environment.

3.2. Variance indicator

There are several processes in a (uncertain) dynamical systems that can cause the diffusion of trajectories over time. This diffusion is characterised by an increase in the variance of the spatial distribution of the trajectories [29]. Diffusion in celestial mechanics has been studied before for several different types of processes, see e.g. [30,31]. In [32,33], and [14], it was found that by studying the coefficients of a polynomial expansion of the uncertain quantity, the effect of diffusion on the variance of the trajectories can be studied in more detail. This work uses this result to develop a dynamics indicator that is based on the variance of the trajectories calculated from the coefficients of the polynomial approximation resulting from the GIPA method.

For an orthogonal polynomial basis $\{\boldsymbol{\Psi}_i\}$, the statistical moments of the uncertainty set can be calculated from the values of the coefficients. First, the mean of the set can be derived as follows:

$$\bar{x}(t) = \mathbb{E}[x(t)] \approx \mathbb{E}[P_{n,d}(\boldsymbol{\xi})] \quad = \int_{\Omega_{\xi}} \left(\sum_{i,|i|\leq n} c_i(t) \boldsymbol{\Psi}_i(\boldsymbol{\xi}) \right) \rho(\boldsymbol{\xi}) d\boldsymbol{\xi} = c_0, \tag{16}$$

where the fact that $\Psi_0 = 1$ and $\mathbb{E}[\Psi i] = 0$, $\forall i \neq 0$ is used to obtain the result. Using Eq. (16), the covariance matrix can be calculated:

$$\Sigma_{\boldsymbol{x}}(t) = \mathbb{E}[(\boldsymbol{x}(t) - \bar{\boldsymbol{x}}(t))^2] \tag{17}$$

$$\approx \int_{\Omega_{\xi}} \left(\sum_{i,|i|\neq 0} \boldsymbol{c}_i(t) \boldsymbol{\Psi}_i(\boldsymbol{\xi}) \right) \cdot \left(\sum_{i,|i|\neq 0} \boldsymbol{c}_i(t) \boldsymbol{\Psi}_i(\boldsymbol{\xi}) \right) \rho(\boldsymbol{\xi}) d\boldsymbol{\xi} \tag{18}$$

$$= \sum_{\boldsymbol{i},\boldsymbol{i}\neq \boldsymbol{0}} \mathbb{E}[\boldsymbol{\Psi}_{\boldsymbol{i}}^2] \, \boldsymbol{c}_{\boldsymbol{i}}(t) \boldsymbol{c}_{\boldsymbol{i}}^T(t), \tag{19}$$

where $\boldsymbol{c}_{\boldsymbol{i}}$ is a vector containing the specific coefficients for each state variable.

As discussed in Section 3.1, this work uses a Taylor basis for the propagation of the uncertainties. As this basis is not orthogonal, the calculation of the variance cannot be performed as in Eq. (19) [34]. Hence, after the propagation is completed, the Taylor basis is converted to an orthogonal basis, namely the Hermite basis. The Hermite basis is orthogonal under the weight function $\rho(x) = e^{-\frac{x^2}{2}}$:

$$\int_{-\infty}^{\infty} H_n(x) H_m(x) \rho(x) dx = n! \sqrt{2\pi} \delta_{nm}, \tag{20}$$

where δ_{nm} is the Kronecker delta function. This basis is selected because of the existence of an analytical relation between the Taylor polynomial (given by a monomial) and the Hermite polynomial, given as follows [35]:

$$x^n = n! \sum_{m=0}^{n/2} \frac{1}{2^m m! (n - 2\,m)!} H_{n-2m}(x), \tag{21}$$

Using the new polynomial basis and the results from Eq. (19), the variance can be found from the corresponding covariance matrix entry as follows:

$$\sigma_{x_i}^2(t) = \Sigma_{\boldsymbol{x}_{ii}}(t) = \sum_{\boldsymbol{i},|\boldsymbol{i}|\neq 0} |\, \boldsymbol{i}\, |! \sqrt{2\pi}\, c_{\boldsymbol{i}}^2(t). \tag{22}$$

In further calculations of the variance, the factor $|\, \boldsymbol{i}\, |! \sqrt{2\pi}$ is ignored as this remains constant between different initial conditions, and therefore does not influence the difference in the variance between the different initial conditions. Taking the maximum variance from the covariance matrix will give the maximum amount of diffusion in the direction of the state variables. Thus, in this work the maximum value of the variance at the final time, i.e.:

$$\eta_{\sigma} = \max_i \sigma_{x_i}^2(t_f), \quad i = 1, 2, \ldots, d \tag{23}$$

is used as an indicator to analyse the increase in variance for different initial conditions.

The variance of Eq. (22) is based on the variance of the Cartesian state variables. However, it can be generalised to a state vector

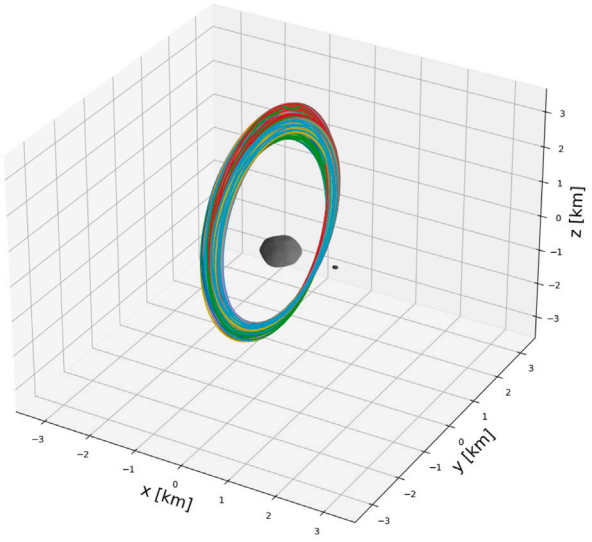

(a) Sample orbits E.

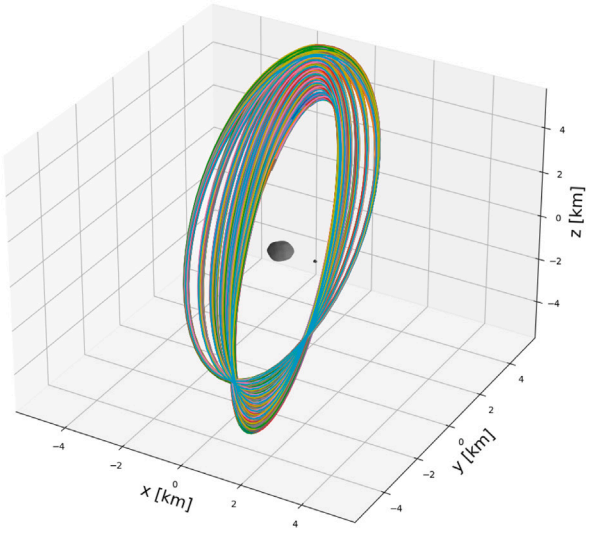

(b) Sample orbits F.

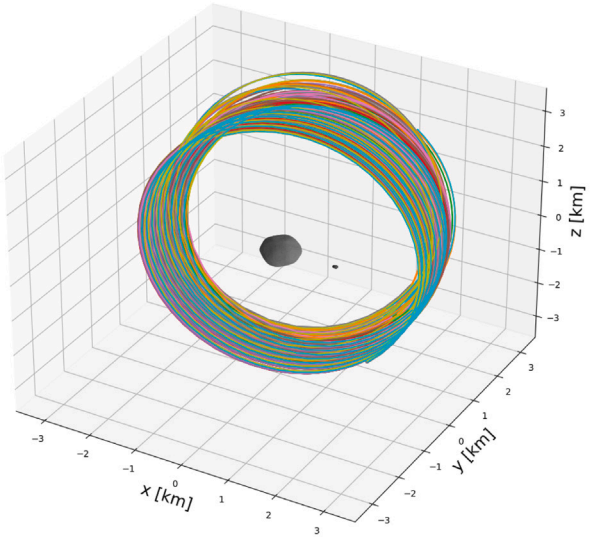

(c) Sample orbits G.

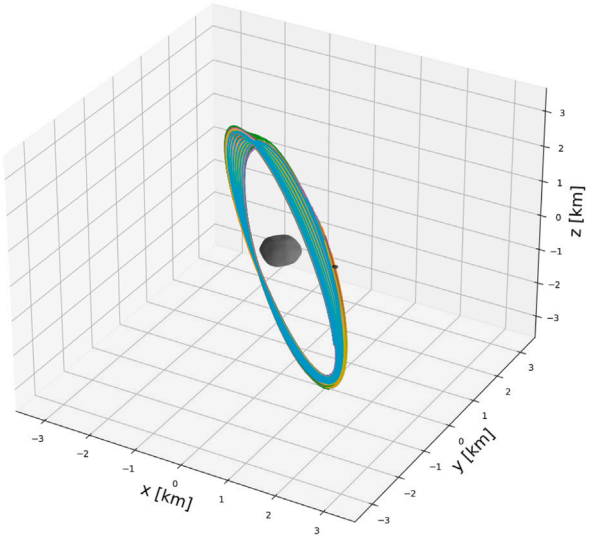

(d) Sample orbits H.

Fig. 6. Sample trajectories from the uncertain dynamics indicator maps propagated until $t_f = 8$ periods for grid 2 and 3.

containing different representations of the state. The Keplerian orbital elements, i.e. the semi-major axis a, eccentricity e, inclination i, argument of perigee ω, and right ascension of the ascending node Ω, can give an intuitive view of the geometry of an orbit around the system. From the mission design perspective, having an orbit with these elements staying relatively bounded over time and are not sensitive to off-nominal conditions is important as this allows for predictable behaviour and low chances of impact or escape. However, in a highly non-linear and uncertain system, like the one considered here, this is not always the case and the variance of the possible orbital elements can grow quickly over time. Therefore, it is important to look at the evolution of these orbital elements and determine if they remain relatively bounded over time. Specifically, the a and e have a large effect on the shape of the orbit and are thus important elements that need to stay relatively constant over time.

Using the same principle as the coefficient based variance for a general state vector, the diffusion of a and e can be calculated. Using the operations defined by the GIPA method, the polynomial approximations of the state variables can be converted to polynomial approximations of a and e using the well-known conversions [36]:

$$a = \frac{1}{\frac{2}{r} - \frac{v^2}{\mu}} \tag{24}$$

$$\boldsymbol{e} = \frac{\boldsymbol{v} \times \boldsymbol{h}}{\mu} - \frac{\boldsymbol{r}}{r}, \tag{25}$$

where μ is the gravitational parameter of the central body (Didymos) and $\boldsymbol{h} = \boldsymbol{r} \times \boldsymbol{v}$ is the angular momentum. The eccentricity can then be obtained by taking the vector norm of Eq. (25). However, a problem arises when the norm is taken of $\boldsymbol{e}$ when the final orbit is close to circular, as a Taylor approximation of a square root around zero

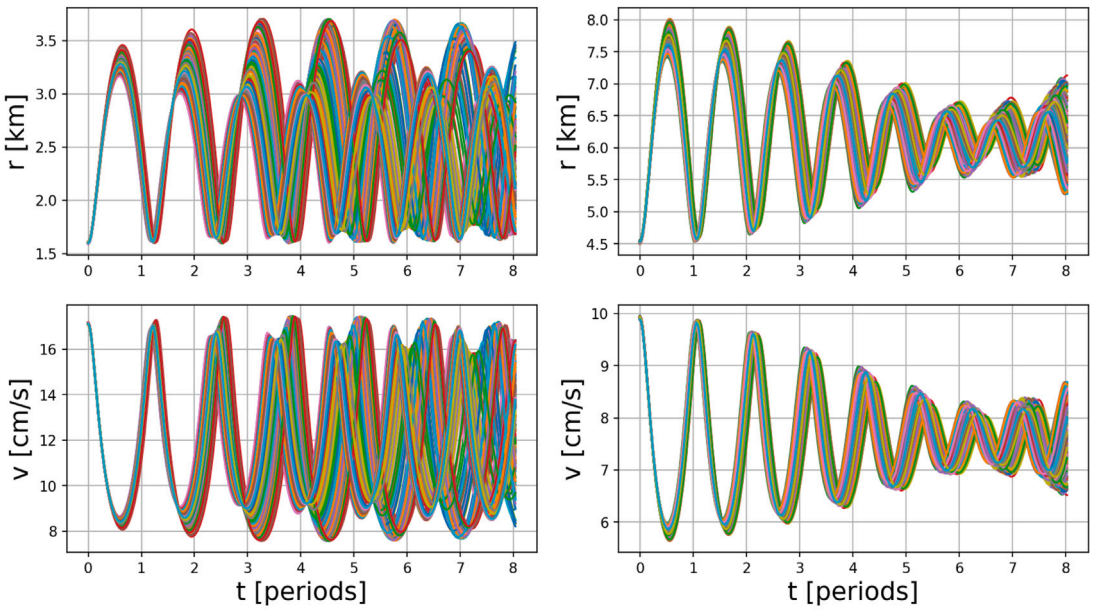

(a) Sample orbits E. (b) Sample orbits F.

Fig. 7. The distance r from the centre of Didymos and velocity v of different trajectories over time for sample orbits E and F.

diverges. Thus instead the squared eccentricity, $|e|^2 = e_1^2+e_2^2+e_3^2$ is used instead. Using Eq. (22), the variance in a and e^2 can then be calculated, representing the diffusion of the shape-based orbital elements.

3.3. $n+1$ Indicator

The accuracy of the Taylor approximation of the dynamics depends on several characteristics of the system. In [37], it was found that an increase in the size of the uncertainty set over time leads to a less accurate polynomial approximation of the set, due to the truncation of the polynomial at a certain degree.

Given a degree n Taylor approximation $P_{n,d}(\boldsymbol{x})$ of the function f around the origin, where f is $n+1$ times differentiable and the $(n+1)$th derivative of f is bounded as follows: $f(\boldsymbol{a})^{(n+1)} \leq M,\ \boldsymbol{a} \in (0, \boldsymbol{x})$, the error bound in the approximation because of the truncation at degree n can be obtained as follows:

$$| f(\boldsymbol{x}) - P_{n,d}(\boldsymbol{x}) | \leq \frac{M}{(n+1)!}\boldsymbol{x}^{n+1} = c_{n+1} \cdot \boldsymbol{x}^{n+1}. \tag{26}$$

As f represents the dynamics of the system, and the $n+1$ coefficient is related to the $(n+1)$th derivative of f in the region over which the Taylor approximation is performed, the specific value of this coefficient can give information on the dynamical behaviour in that region. The specific value of c_{n+1} can be affected by several different factors, e.g. the propagation time, initial uncertainty size, and the non-linearity of the system [37]. It can be seen that for a Taylor approximation with a high c_{n+1}, trajectories that start close together in the domain of the Taylor approximation can have significantly different behaviours.

An example illustration of this effect is shown in Fig. 2. Two sets, A and B, are propagated through two different dynamics (this can be two different dynamical systems or two different regions in phase space of the same system). At t_f, the shape of set A has been significantly deformed because of the non-linearity of the dynamics. Set B has grown larger compared to set A but has been deformed less, due to the more linear dynamics which can only cause a rotation and expansion (or contraction) of the set. Hence, a low degree n polynomial can accurately approximate set B as there are no higher order, non-linear effects, which causes c_{n+1} to be small. If the same order n is used for the approximation of set A, the error in the approximation would be high as higher order terms are needed to capture the non-linear effects that cause this deformation. This leads to a high value of c_{n+1} in this case. Therefore, fixing the degree n of the polynomial approximations (keeping the degree high enough to accurately approximate most of the phase space) and comparing the values of c_{n+1} for different regions of phase space gives the relative non-linearity of those regions.

The non-linearity of the system, measured by c_{n+1}, can indicate chaotic or diffusive behaviour. However, it is noted that they are not necessarily directly related to each other. For example, in a system where certain close initial conditions behave significantly different from each other, but over time remain confided in a certain region of phase space (e.g. a strange attractor), the non-linearity would be high but the diffusion would be low. Therefore, it is important to measure both the variance indicator and the non-linearity indicator as they give different insights into the dynamics and can be combined to get a better idea of the robust stability.

In [38], the maximum initial set size for a Taylor approximation was calculated using the estimated truncation error, and used as a dynamics indicator for the circular restricted three body problem. Furthermore, in [11] a Taylor algebra with a truncation error based domain splitting technique was used as an indicator of the stability of certain orbits under uncertainties, by measuring the amount of splits at a specific location in phase space. In this work a similar approach is used, namely the size of the $n+1$ degree coefficients is used as an indicator to determine suitable initial conditions for robust stable orbits. This method avoids the use of methods like automatic domain splitting, which decreases the efficiency and ease-of-use of GIPA.

The size of the $n+1$ degree coefficients is calculated as follows. First, a set of initial conditions and model parameters is propagated using the GIPA method. Second, from the resulting polynomial approximation, the size of the coefficients of a specific degree i are calculated, up to polynomial degree n as follows:

$$S_i = \sum_{|\boldsymbol{i}|=i} c_i. \tag{27}$$

Using the values of S_i for all the different degrees up to and including n, a least-squares fit algorithm is used to get an analytical expression for the size of the coefficients for a specific degree. To improve the accuracy and efficiency of the fitting procedure, a linear fit is performed using the equation as follows:

$$\log S_i = \log A - B \cdot i, \tag{28}$$

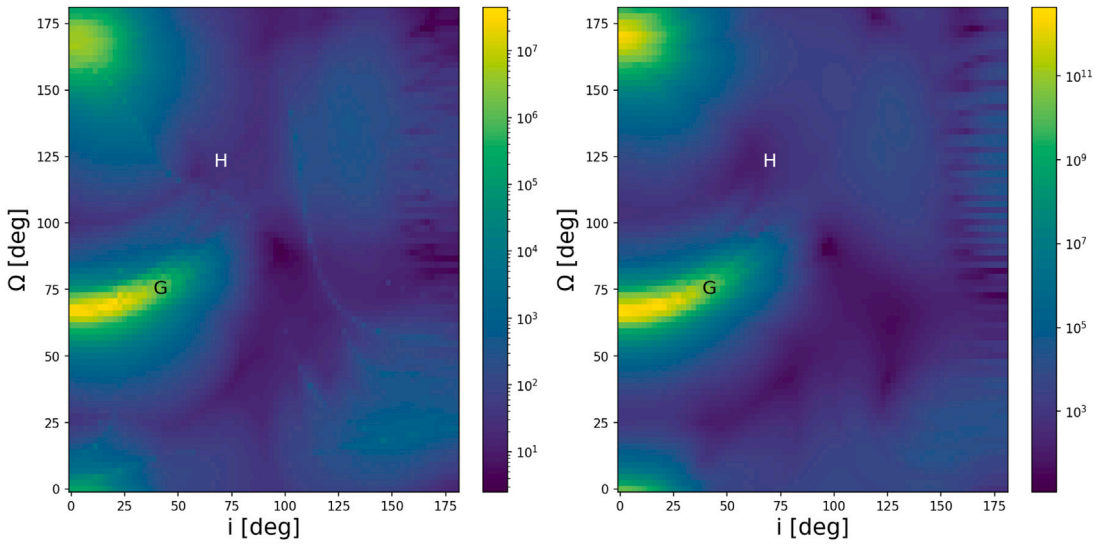

(a) η_{n+1}. (b) η_{σ}.

Fig. 8. The uncertain dynamics indicators for grid 3. The colourmaps represent the value of the respective indicator, thus the amount of variance and non-linearity.

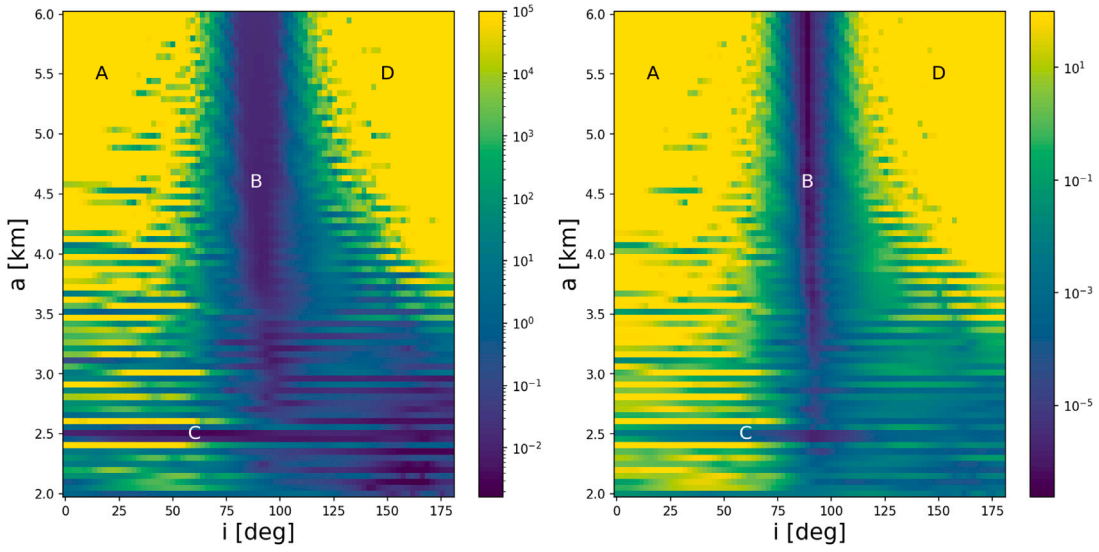

(a) Variance in a. (b) Variance in e^2.

Fig. 9. The variance in the semi-major axis a and squared orbital eccentricity e^2 at the final time for grid 1. The letters indicate the set of sample orbits that are used to verify this grid, which are shown in Fig. 4.

where A and B are constants estimated using the least squares algorithm. Finally, using Eq. (28), the value for the $n+1$ degree coefficient size, S_{n+1}, can be estimated.

As the $S_{n+1,j}$ represents the $n+1$ coefficient size for each different state variable, the direction of maximum non-linearity can be found by taking the maximum value of $S_{n+1,j}$ over all state variables. This value is then used as the indicator as follows:

$$\eta_{n+1} = \max_j S_{n+1,j}, \quad j = 1, 2, \dots, d \tag{29}$$

4. Observability analysis

From the perspective of mission operations, the robust stability discussed in Section 3 is an important factor in the selection of an orbit for a spacecraft as it shows how frequent adjustments need to be made to the trajectory to keep it within the desired bounds. In addition, the spacecraft needs to fulfil a certain set of operational and scientific requirements that are influenced by the specific orbit the spacecraft is in. In previous studies [3,8,39] the different constraints and requirements for the trajectory design of the different spacecraft orbiting Didymos and observe Dimorphos are discussed. One of the main important factors that is discussed is the observability of Dimorphos in terms of lighting for the passive instruments (e.g. optical cameras).

To determine the observability of Dimorphos, several key factors need to be taken into account [40]. These factors are all related to the illumination and geometry of the system. It is required for several instruments on-board the spacecraft to observe the body with sufficient illumination to determine all the necessary features. First, the angle between the lines connecting the Sun and Dimorphos, and the spacecraft and Dimorphos is calculated (i.e. the phase angle). If this angle is smaller then 90 degrees, the illumination is sufficient. Second, it is determined whether Dimorphos is located in the shadow of Didymos, where the shape of the shadow is taken to be conical. Finally, it is determined whether Dimorphos is not located behind Didymos with

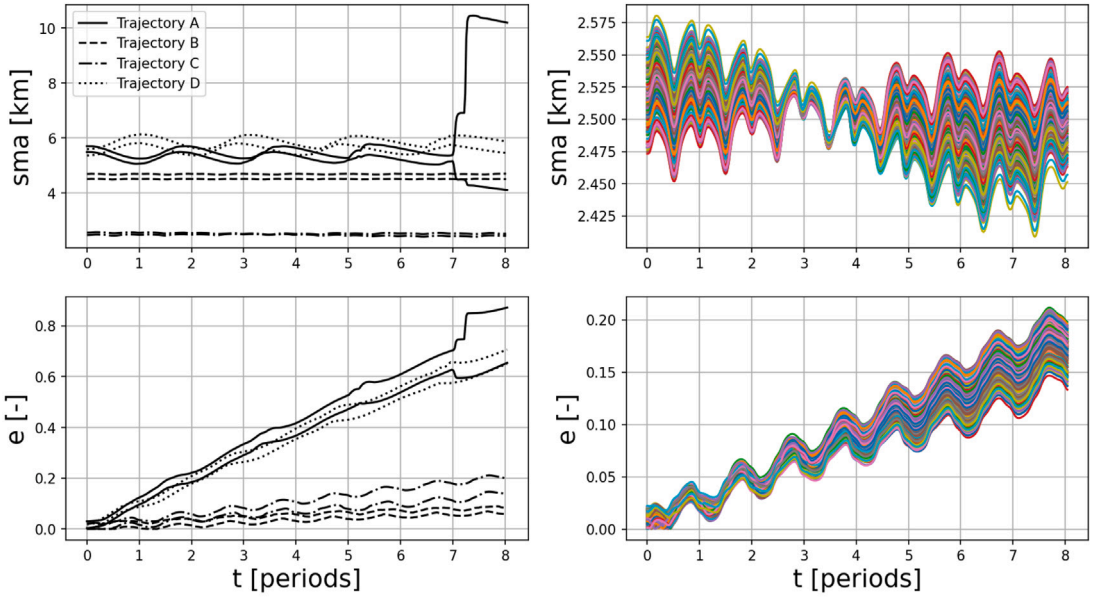

(a) Orbital elements bounds. (b) Sample orbits C.

Fig. 10. Maximum and minimum values for the semi-major axis and eccentricity of the different initial conditions and the sample orbits shown for C.

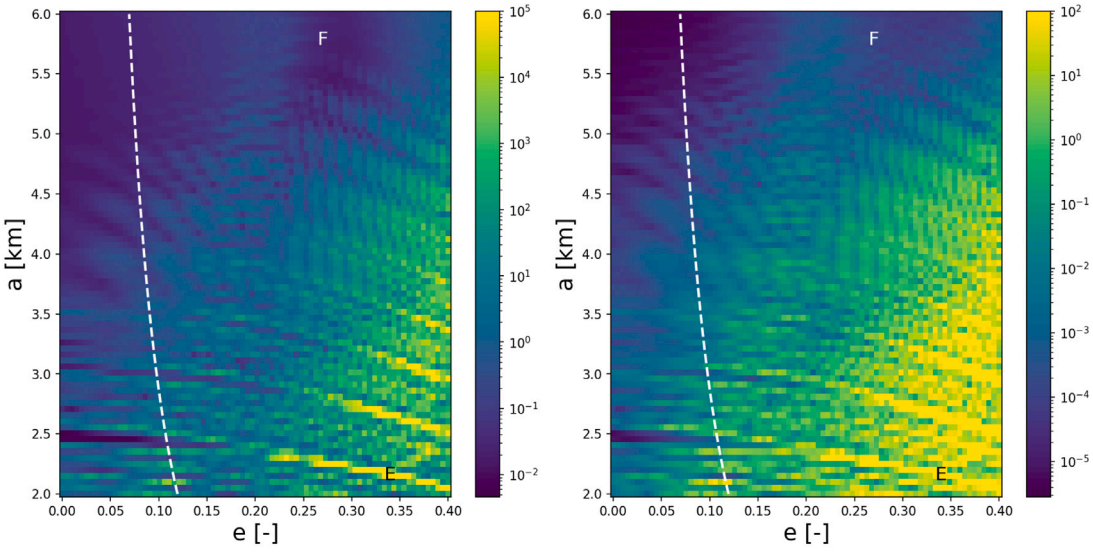

(a) Variance in a. (b) Variance in e^2.

Fig. 11. The variance in the semi-major axis a and squared orbital eccentricity e^2 at the final time for grid 2. The dotted line represents the theoretical frozen orbit condition from Eq. (30).

respect to the position of the spacecraft. At all evaluation points in an orbit, these three factors are calculated. If they are all shown to be favourable (i.e. Sun angle less then 90 degrees, not in shadow, and Didymos is not blocking Dimorphos), then at that time Dimorphos is deemed observable. If any of these factors are determined to be false, then Dimorphos is not observable. At the end of a simulation run, the percentage of time Dimorphos is observable is calculated. This measure of observability is similar to the one used for the trajectory design of the close proximity phase of the Hera spacecraft [41].

Table 2
The initial conditions for the three different maps.

Parameter	Grid 1	Grid 2	Grid 3
a [km]	[2–6]	[2–6]	3
e [-]	0	[0–0.4]	0
i [°]	[0–180]	85	[0–180]
Ω [°]	90	90	[0–180]
ω [°]	−90	−90	−90
ν [°]	0	0	0

5. Orbit analysis

The uncertain dynamics are investigated for a set of initial conditions that are generated from a range of Kepler orbital elements. As this is a highly perturbed environment, these orbital elements will quickly diverge from the classical two-body values (or their original values) and thus are only used to generate a set of interpretable initial conditions and to understand the evolution of the shape of the orbit over time.

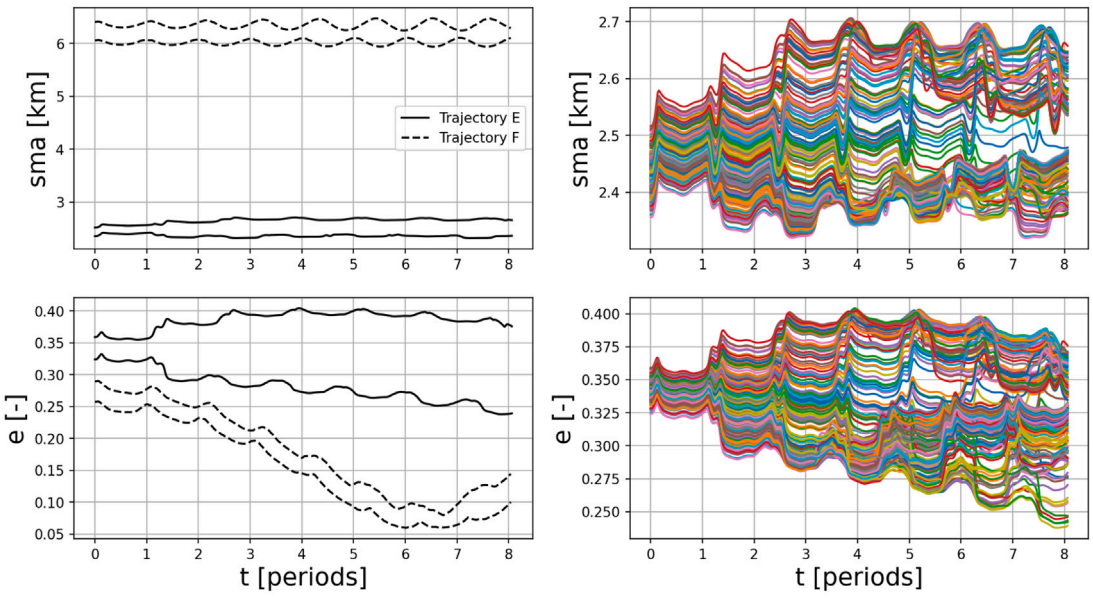

(a) Orbital elements bounds. (b) Monte Carlo results for E.

Fig. 12. The orbital elements over time for two different test trajectories from grid 2. In 12(a) the bounds are shown, and in 12(b) the results for E are shown in more detail.

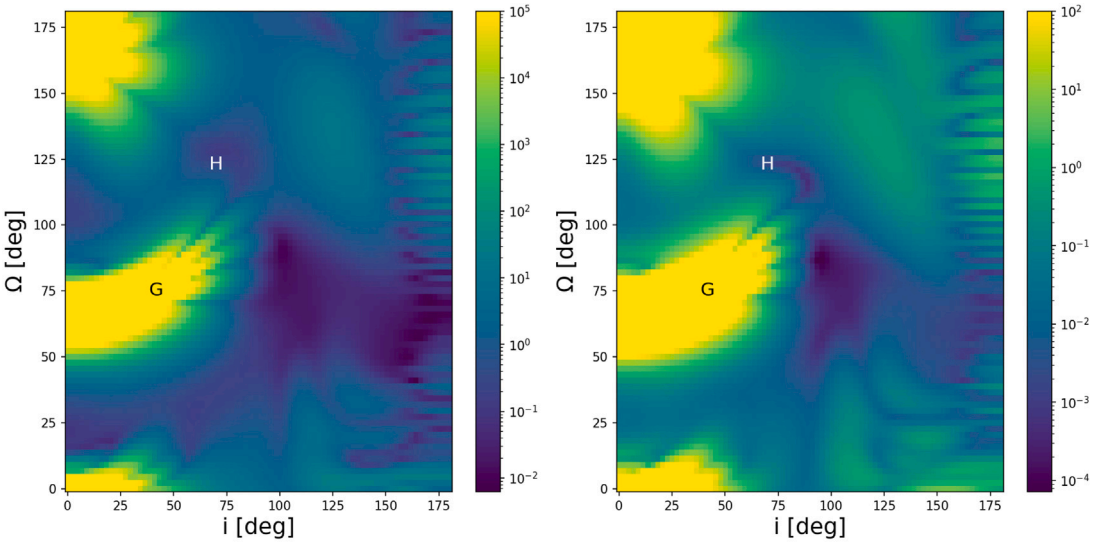

(a) Variance in a. (b) Variance in e^2.

Fig. 13. The variance in the semi-major axis a and squared orbital eccentricity e at the final time for grid 3.

The initial orbital elements are converted to Cartesian coordinates to perform the integration. Three grids of 80 by 80 points are constructed from the different initial conditions. For each grid two orbital elements vary and the other orbital elements remain constant. The specific initial conditions for each grid are shown in Table 2. The first grid investigates the effect of a and i for circular orbits facing the Sun. The second grids focuses specifically on the terminator orbits and the effect of e. Finally, for a fixed a the orbital plane is varied with a grid in i and Ω.

Each point on the three different grids is propagated for five orbital periods (calculated from the initial a), using a Runge–Kutta 4 numerical integrator. Uncertainties are considered in the initial state (position and velocity), C_{20}, C_{22}, and the spacecraft SRP force. The SRP uncertainty stems from both uncertainty in the parameters and inaccurate modelling of this force. However, GIPA works with individual uncertain variables, hence only parameter $1/B$ is considered to have an uncertainty in this case, and the inaccurate modelling is not considered for this analysis. The uncertainty of the parameter $1/B$ is directly proportional to the uncertainty in the final acceleration for the Cannonball SRP model, and can thus represent the total uncertainty in the SRP force. The state uncertainties are set to a value of 1 percent to be able to determine the effect of small perturbations in the state. The model parameters, i.e. C_{20}, C_{22}, and B will have a larger uncertainty of 10 percent, representing the possible values these parameters can take. Furthermore, a polynomial degree of 5 is selected as this has previously been shown to be a good trade-off between speed and accuracy [27]. All values used during propagation are adimensionalized and scaled by dividing them by the position and period of Dimorphos with respect to Didymos, based on their respective units. This improves the numerical efficiency of the integration. Hence, all the indicator values do not have a unit as well. As the indicators are mainly used in maps to compare their relative values and find regions of relatively robust stability, their absolute values are of less significance.

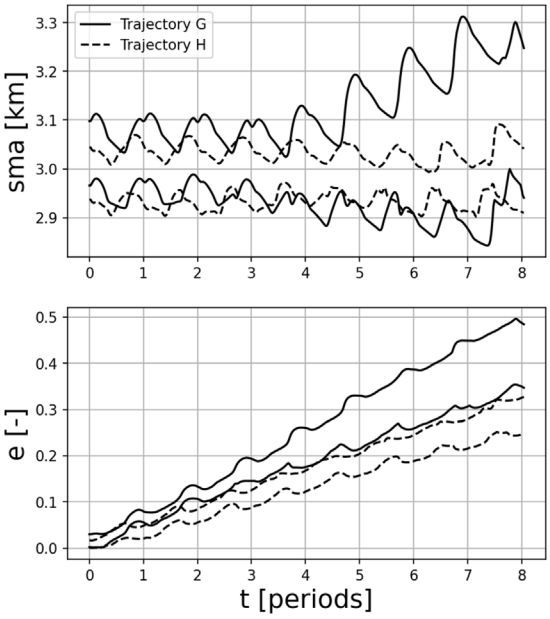

Fig. 14. Maximum and minimum values for the semi-major axis and eccentricity of the sample orbits from grid 3.

5.1. Robust stability maps

Fig. 3 shows the result for the η_{n+1} indicator and the η_σ indicator for grid 1. Where the Cartesian state is considered for the η_σ indicator. The colours in the two plots represent the values of the variance η_σ and non-linearity η_{n+1} indicator. Lower values of both these indicators means in general that those initial conditions are less sensitive to changes in both the initial conditions and dynamical parameters, and thus these trajectories remain more closely bounded. Hence, they can generally be viewed as being more robust stable than regions with higher values of the indicators, according to the definition given in Section 3.

Several general regions of interest can be found in these maps. First, the prograde and retrograde orbits ($<\sim 90°$ and $>\sim 90°$ respectively) at larger a show unstable behaviour. For these regions, the SRP is of a similar order with the gravitational force and therefore has a significant destabilising effect on these orbits. Due to this sensitivity to the SRP, the uncertainty in the B parameter increases the diffusion of these trajectories as well. Closer to the system, the retrograde orbits become more stable as the SRP force becomes less significant compared to the gravity of both bodies. However, the prograde orbits remain relatively unstable compared to the retrograde ones. The retrograde orbits experience less influence from the non-spherical gravity contributions due to the high relative velocities with respect to the asteroid. This also means that the uncertainties in the C_{20} and the C_{22} value have less of an influence on these trajectories. Closer to the body, the influences of both the resonances with the spin of the primary and the orbital motion of the secondary can be observed in the maps (2:1 mean motion resonance at 2.1 km and the 3:1 orbital resonance at 2.475 km). These resonances in combination with the uncertainties in the gravity field can be seen to cause both stable and unstable behaviour. The most stable behaviour can be found around the terminator orbit, which corresponds to previously found results, e.g. [42], showing that these orbits are robust against uncertainties in the gravity field and SRP force.

To validate the map of grid 1, a Monte Carlo analysis with 1000 samples for a longer period of time of 8 orbital periods of the spacecraft is performed for four different initial conditions shown in Fig. 3. The resulting trajectories are shown in Fig. 4 using different colours for the different Monte Carlo samples. From the robust stability grids, the two trajectories A and D are expected to be unstable, which is proven by the diffusive behaviour among the different sample trajectories and by the rapid change of the eccentricity and semi-major axis over time of most sample trajectories. Furthermore, the two stable trajectories B and C have significantly less diffusion and remain close to the initial orbit.

Finally, the results for grid 3 can be seen in Fig. 8. For these maps there is a more clear difference between the η_{n+1} and η_σ indicators, as there are several regions and structures in the η_{n+1} map which do not appear in the η_σ map. From the discussion in Section 3.3, it is observed that η_{n+1} is an indicator of the non-linearity, which is not strictly affected by the diffusion. Hence, it is possible that these factors increase the η_{n+1} more for these regions and structures, therefore changing the relative value.

The two main regions of unstable motion are similar between the two indicators. They can be found in the range of $i \approx [20°–70°]$, $\Omega \approx [40°–90°]$ and for $i \approx [0°–20°]$, $\Omega \approx [125°–175°]$. Various robust stable structures can be found in these maps. As can be seen from Fig. 3, the value of a used for this map is close to the transition where the SRP force becomes less dominant and the non-spherical shape become more dominant, as the retrograde orbits go from unstable to stable. This leads to various different robust stable combinations of i and Ω.

Two sample initial conditions, G and H, are taken from the two maps and analysed using a Monte Carlo analysis. The results can be seen in Figs. 6(c) and 6(d). These analyses match with the expected robust stability as around G the trajectories diffuse more compared to H.

Besides the η_σ indicator for the variance in the Cartesian state, the variance in a and e is also measured. These indicators are shown for grid 1 in Fig. 9. These maps show how the bounds of the orbital elements evolve over time due to sensitivity to the state and model parameters. It can be seen that in general these results agree with the robust stability indicators from Fig. 3. The orbital elements a and e remain the most bounded for terminator orbits and close (< 3 km) retrograde orbits, whereas the orbits with a high influence of the SRP show high variance.

The results from Fig. 9 can be verified using a similar MC method as was discussed before. The same sample points, A to D, are used (see Fig. 9) and the spread and evolution of the trajectories from the Monte Carlo analysis are investigated in more detail. The bounds of the orbital elements for the four sample regions are shown in Fig. 10(a). As expected, the bounds of a and e for A and D are both increasing over time, whereas for B and C these remain much more constant. For C (around the 3:1 orbital resonance), the bounds of a seem to shrink until 3 orbital periods is reached after which the bounds increase again as can be seen in Fig. 10(b). These results agree with what is expected from the maps developed in Fig. 9.

The same similarity between the robust stability indicators and the variance in a and e of grid 1 can be found for grid 2 in Fig. 11. The main difference in the variance maps is that the contrast for regions of high and low robust stability is greater for the orbital elements maps compared to the Cartesian maps. This shows the sensitivity of the orbital bounds to the effect of the uncertain dynamics in different regions of initial conditions. In [42], an analytical estimate of the eccentricity as a function of semi-major axis for a stable terminator orbit conditions was derived as :

$$e = \cos \Lambda, \tag{30}$$

$$\tan \Lambda = \frac{3(1+\kappa_s)P_0}{2B}\sqrt{\frac{a}{\mu_{did}\mu_{Sun}a_H(1-e_H^2)}}, \tag{31}$$

where a_H and e_H are the heliocentric semi-major axis and eccentricity. This function is shown in the maps of Fig. 11 as a white dotted line. It can be seen that for a larger a, this theoretical value is located in the region with the low η_σ and low η_{n+1} region, thus it still is able to predict the stable e values well. As the orbit gets closer to the system, other unmodelled perturbations like the gravity of Dimorphos reduce the accuracy of Eq. (30) and thus show more unstable behaviour.

The orbital element bounds for sample orbits from E and F are shown in Fig. 12. The stable region F has relatively constant bounds

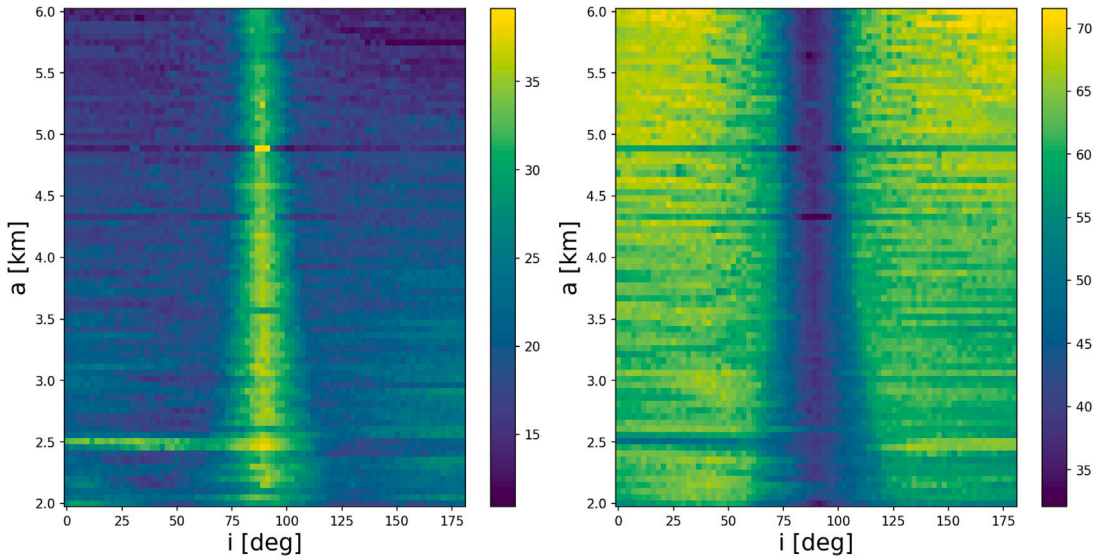

(a) Minimum observability. (b) Maximum observability.

Fig. 15. Minimum and maximum observability, shown in percentage of the trajectory for which Dimorphos is observable for grid 1.

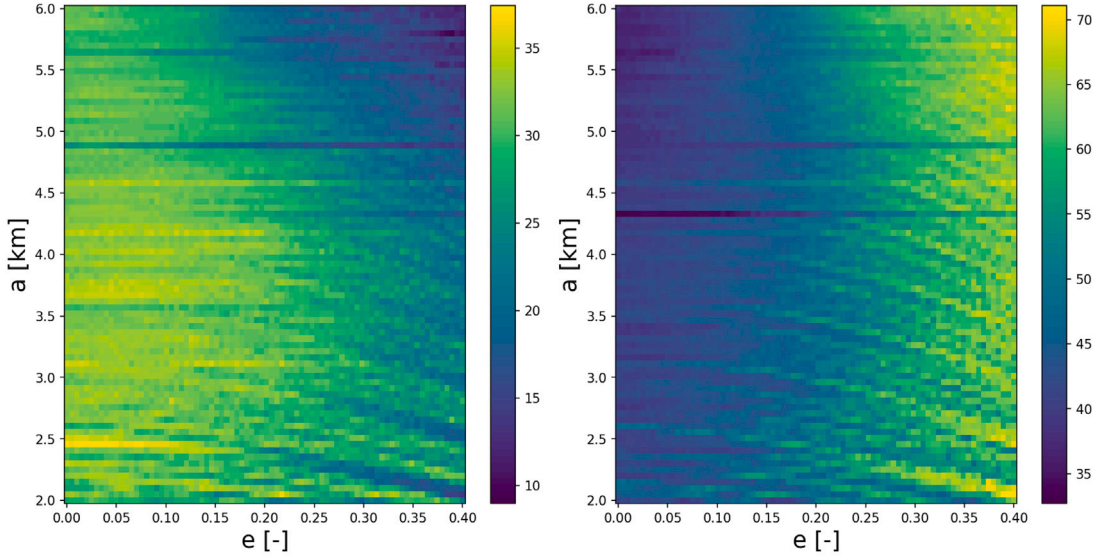

(a) Minimum observability. (b) Maximum observability.

Fig. 16. Minimum and maximum observability, shown in percentage of the trajectory for which Dimorphos is observable for grid 2.

and also has a decreasing mean value for e. In contrast, the bounds for E are growing slowly. Furthermore, due to the orbital resonance around this initial condition, an empty region is found after around 4 periods. This resonance alters the orbits around this region to form two different groups.

For grid 3, the results are shown in Fig. 13. The highest values for the variance of a are lower compared to the previous maps, showing some more structure in both the unstable and stable regions. It can be seen that there are several structures of stable behaviour within the unstable regions. Furthermore, the region around $i = 180°$ shows the lowest variance in the orbital elements, representing regions of bounded motion.

The bounds for the sample orbits in Fig. 14 show again the difference between the stable and unstable region. The difference is relatively small for a. However, for e it can be seen that the difference in both the growth of the mean and variance is larger. The maps show as well that the effect of Ω is more significant for the prograde motion, where more regions of high variance are found.

The analysis performed using the indicators in this section does not directly measure the safety against impact, as the time period over which the polynomial propagation is performed is not long enough to find impact trajectories. However, for Monte Carlo analyses of several unstable orbits for longer periods of time (e.g. Fig. 4(a)), several orbits were found to impact with one of the asteroids in the system. Therefore, it is implied here that orbits from regions of high indicator values of the robust stability maps have a higher risk in terms of possible impacts. A more quantitative analysis of this impact risk is left for future work.

5.2. Secondary asteroid observability

To test the ability of this method to analyse the mission parameters and performance, the observability for the three grids is measured.

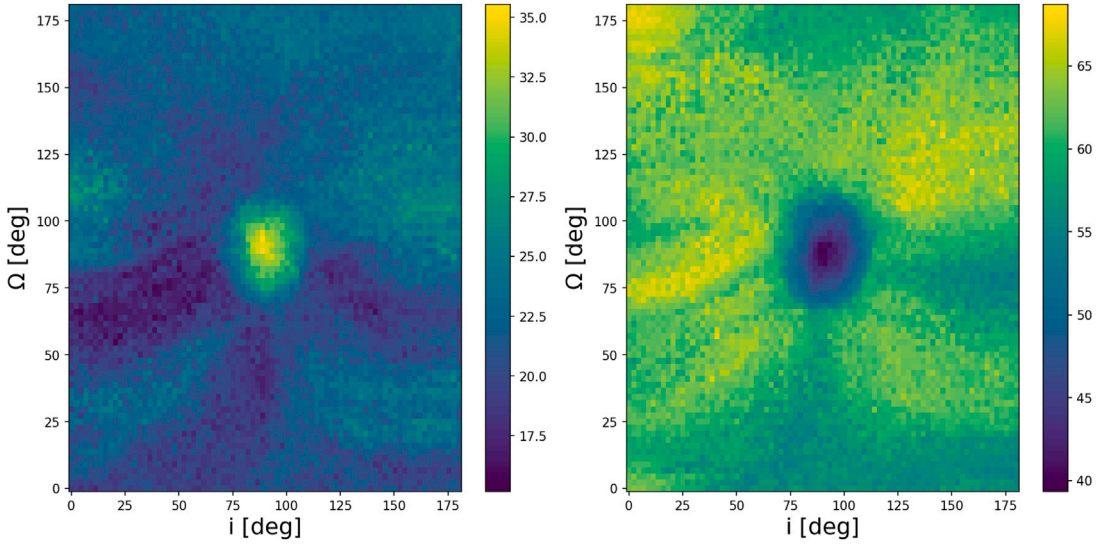

(a) Minimum observability. (b) Maximum observability.

Fig. 17. Minimum and maximum observability, shown in percentage of the trajectory for which Dimorphos is observable for grid 3.

The upper and lower bounds for the observability is shown in Fig. 15 for grid 1. The stability of the region around the terminator orbit makes the bounds of the observability lie close together (30–50 percent). The unstable regions allow for both lower minimal values (higher chance of bad observability conditions), but also higher maximum values (higher chance of good observability). This is caused by the diffusion of trajectories allowing for a wider spread of trajectories with different geometries. Part of these trajectories allow for better observability conditions. Therefore, from these plots a trade-off can be made among the robust stability and boundedness shown in Figs. 3 and 9, and the observability of the secondary in Fig. 15.

The same effect can be seen for grid 2 in Fig. 16. However, there is a much larger difference between the uncertain dynamics maps and the observability maps for grid 3, as is shown in Fig. 17. The terminator orbit is again shown here to have much smaller difference between the maximum and minimum bounds, indicating that the geometry for these orbits is less sensitive to state and model parameter uncertainties. Due to these small bounds, the terminator orbits minimise the worst case scenario observability while also lowering the maximum possible observability. The coverage of Dimorphos was not taken into account for this analysis, however it is noted here that the terminator orbits tend to observe the same face of the asteroid, reducing the coverage of the body from these orbits [41].

6. Conclusion

In this paper, a novel method of determining the robust stability is applied to study the dynamics under uncertainties around the Didymos system. This method uses a polynomial expansion together with an algebra over the space of the polynomials to calculate the evolution of an uncertainty set through the dynamical system. A set of different uncertain dynamics indicators, which are derived from the polynomial coefficients, are then used to determine the relative robust stability between the different orbits.

Using these indicators, it is shown that the terminator and close retrograde orbits show robust stable behaviour. This corresponds with previous results (e.g. [22]) which also found that these types of orbits are stable. This verifies the ability of the indicators to find robust stable orbits, and thus allows for the further study of other features of the uncertain dynamics. When the motion is close to the body, the stability of the terminator orbit is not guaranteed as the dynamical structure becomes more complex due to the effect of the non-spherical gravity, the uncertainties in C_{20} and C_{22}, and the presence of resonances with Dimorphos' orbit. Furthermore, slightly eccentric terminator orbits show stable behaviour for higher semi-major axes (corresponding to previous analytical predictions [42]), but the range of stable eccentricities decrease if the semi-major axis decreases. Finally, several different stable regions besides the terminator plane were found when changing the ascending node and inclination, allowing for different options when the terminator orbit is not desirable.

Additionally, the performance of certain orbits in terms of the observability of Dimorphos are analysed. It is found that in general the stable regions show smaller bounds for the observability, minimising the worst case scenario but also not allowing the maximum observability to become larger compared to other initial conditions. This is especially the case for the terminator orbits, showing less favourable geometry for the maximum observability.

For future work, more potential initial conditions can be considered, e.g. quasi-satellite orbits. Furthermore, improvements in terms of the η_{n+1} indicator to separate the effects of the diffusion and non-linearity could increase its effectiveness and the amount of information that can be extracted from this indicator.

Declaration of competing interest

The authors declare that they have no known competing financial interests or personal relationships that could have appeared to influence the work reported in this paper.

Acknowledgements

The authors would like to acknowledge the ESA OSIP program for partly sponsoring this research project. Furthermore, the authors are grateful to Jesus Gil-Fernandez for his help and advice, and Cristian Greco for his insights on the GIPA method.

References

[1] P. Michel, M. Küppers, A.C. Bagatin, B. Carry, S. Charnoz, J. d. Leon, A. Fitzsimmons, P. Gordo, S.F. Green, A. Hérique, M. Juzi, O. Karatekin, T. Kohout, M. Lazzarin, N. Murdoch, T. Okada, E. Palomba, P. Pravec, C. Snodgrass, P. Tortora, K. Tsiganis, S. Ulamec, J.-B. Vincent, K. Wünnemann, Y. Zhang, S.D. Raducan, E. Dotto, N. Chabot, A.F. Cheng, A. Rivkin, O. Barnouin, C. Ernst, A. Stickle, D.C. Richardson, C. Thomas, M. Arakawa, H. Miyamoto, A. Nakamura, S. Sugita, M. Yoshikawa, P. Abell, E. Asphaug, R.-L. Ballouz, W.F. Bottke, D.S. Lauretta, K.J.

Walsh, P. Martino, I. Carnelli, The ESA hera mission: Detailed characterization of the DART impact outcome and of the binary asteroid (65803) didymos, Planet. Sci. J. 3 (7) (2022) 160, [Online]. Available: https://iopscience.iop.org/article/10.3847/PSJ/ac6f52 https://iopscience.iop.org/article/10.3847/PSJ/ac6f52/meta.

[2] F. Ferrari, V. Franzese, M. Pugliatti, C. Giordano, F. Topputo, Preliminary mission profile of Hera's Milani CubeSat, Adv. Space Res. 67 (6) (2021) 2010–2029.

[3] H. Goldberg, o. Karatekin, B. Ritter, A. Herique, P. Tortora, C. Prioroc, B. Gutierrez, P. Martino, I. Carnelli, The juventas CubeSat in support of ESA's Hera mission to the asteroid didymos, in: Small Satellite Conference, 2019, [Online]. Available: https://digitalcommons.usu.edu/smallsat/2019/all2019/73.

[4] D.J. Scheeres, Orbital Motion in Strongly Perturbed Environments, Springer, Berlin Heidelberg, 2012.

[5] F. Damme, H. Hussmann, J. Oberst, Spacecraft orbit lifetime within two binary near-Earth asteroid systems, Planet. Space Sci. 146 (2017) 1–9.

[6] L. Dell'Elce, N. Baresi, S.P. Naidu, L.A. Benner, D.J. Scheeres, Numerical investigation of the dynamical environment of 65803 didymos, Adv. Space Res. 59 (5) (2017) 1304–1320.

[7] H. Shang, X. Wu, P. Cui, Trajectory exploration within asynchronous binary asteroid systems using refined Lagrangian coherent structures, Celestial Mech. Dynam. Astronom. 127 (2) (2017) 185–210, [Online]. Available: https://link.springer.com/article/10.1007/s10569-016-9723-y.

[8] F. Ferrari, V. Franzese, M. Pugliatti, C. Giordano, F. Topputo, Trajectory options for Hera's Milani CubeSat around (65803) didymos, J. Astronaut. Sci. (2021) 1–22, [Online]. Available: https://link.springer.com/article/10.1007/s40295-021-00282-z.

[9] S.P. Naidu, L.A. Benner, M. Brozovic, M.C. Nolan, S.J. Ostro, J.L. Margot, J.D. Giorgini, T. Hirabayashi, D.J. Scheeres, P. Pravec, P. Scheirich, C. Magri, J.S. Jao, Radar observations and a physical model of binary near-Earth asteroid 65803 didymos, target of the DART mission, Icarus 348 (2020) 113777.

[10] J. Feng, X. Hou, R. Armellin, Survey on studies about model uncertainties in small body explorations, 2019, 100549.

[11] J. Feng, D. Santeramo, P. Di Lizia, R. Armellin, X. Hou, Stability indicator of orbital motion around asteroids with automatic domain splitting, in: Proceedings of the International Astronautical Congress, IAC, vol. 2019, 2019.

[12] J. Feng, D. Santeramo, P. Di Lizia, R. Armellin, X. Hou, Dynamical structure of the motion around asteroids with uncertain gravity and solar radiation pressure, Acta Astronaut. 186 (2021) 135–147.

[13] J. Feng, X. Hou, P. Di Lizia, R. Armellin, D. Antonio Santeramo, Sensitivity analysis of the orbital motion around 469219 Kamo'oalewa (2016 HO_3) to uncertainties on asteroid mass and solar radiation pressure, Adv. Space Res. (2021) [Online]. Available: https://linkinghub.elsevier.com/retrieve/pii/S027311772100884X.

[14] I. Fodde, J. Feng, M. Vasile, Uncertainty maps for motion around binary asteroids, Celestial Mech. Dynam. Astronom. 134 (5) (2022) 1–23, [Online]. Available: https://link.springer.com/article/10.1007/s10569-022-10096-2.

[15] Hera Didymos Reference Model Issue 5, ESA, Tech. Rep. 2020.

[16] O. Montenbruck, E. Gill, Satellite Orbits: Models, Methods and Applications, Springer, Berlin Heidelberg, 2000.

[17] G. Balmino, Gravitational potential harmonics from the shape of an homogeneous body, Celest. Mech. Dyn. Astron. 60 (3) (1994) 331–364, [Online]. Available: https://link.springer.com/article/10.1007/BF00691901.

[18] X. Hou, D.J. Scheeres, X. Xin, Mutual potential between two rigid bodies with arbitrary shapes and mass distributions, Celestial Mech. Dynam. Astronom. 127 (3) (2017) 369–395, [Online]. Available: https://link.springer.com/article/10.1007/s10569-016-9731-y.

[19] I. Jean, A.K. Misra, A. Ng, Controlled spacecraft trajectories in the context of a mission to a binary asteroid system, J. Astronaut. Sci. 68 (1) (2021) 38–70, [Online]. Available: https://link.springer.com/article/10.1007/s40295-021-00248-1.

[20] L.E. Cunningham, On the computation of the spherical harmonic terms needed during the numerical integration of the orbital motion of an artificial satellite, Celestial Mech. 2 (2) (1970) 207–216, [Online]. Available: https://link.springer.com/article/10.1007/BF01229495.

[21] C. Bottiglieri, F. Piccolo, A. Rizza, C. Giordano, M. Pugliatti, V. Franzese, F. Ferrari, F. Topputo, Trajectory design and orbit determination of Hera's Milani CubeSat, in: AAS/AIAA Astrodynamics Specialist Conference, 2021.

[22] S. Kikuchi, Y. Tsuda, M. Yoshikawa, K. Jun'ichiro, Stability analysis of coupled orbit-attitude dynamics around asteroids using finite-time Lyapunov exponents, J. Guid. Control Dyn. 42 (6) (2019) 1289–1305, [Online]. Available: https://arc.aiaa.org/doi/abs/10.2514/1.G003879.

[23] B. Villac, S. Broschart, Applications of chaoticity indicators to stability analysis around small bodies, in: Advances in the Astronautical Sciences, vol. 134, 2009.

[24] G. Haller, Lagrangian coherent structures, Annu. Rev. Fluid Mech. 47 (2015) 137–162, [Online]. Available: https://www.annualreviews.org/doi/abs/10.1146/annurev-fluid-010313-141322.

[25] M. Vasile, C.O. Absil, A. Riccardi, Set propagation in dynamical systems with generalised polynomial algebra and its computational complexity, Commun. Nonlinear Sci. Numer. Simul. 75 (2019) 22–49.

[26] A. Giorgilli, M. Sansottera, Methods of algebraic manipulation in perturbation theory, Third Plata Int. Sch. Astron. Geophys. (2013) 147–183, [Online]. Available: http://arxiv.org/abs/1303.7398.

[27] I. Fodde, J. Feng, M. Vasile, Uncertainty propagation for orbital motion around an asteroid using generalized intrusive polynomial algebra: Application to didymos system, in: 8th International Conference on Astrodynamics Tools and Techniques - Virtual, 2021, [Online]. Available: https://pureportal.strath.ac.uk/en/publications/uncertainty-propagation-for-orbital-motion-around-an-asteroid-usi.

[28] C.O. Absil, A. Riccardi, M. Vasile, C. Tardioli, SMART-UQ: Uncertainty quantification toolbox for generalised intrusive and non intrusive polynomial algebra, in: 6th International Conference on Astrodynamics Tools and Techniques, Darmstadt, Germany, 2016, [Online]. Available: https://pureportal.strath.ac.uk/en/publications/smart-uq-uncertainty-quantification-toolbox-for-generalised-intru.

[29] S.B. Alves, G.F. De Oliveira, L.C. De Oliveira, T. Passerat De Silans, M. Chevrollier, M. Oriá, H.L.S. Cavalcante, Characterization of diffusion processes: Normal and anomalous regimes, Physica A 447 (2016) 392–401.

[30] S.N. Sharma, H. Parthasarathy, Dynamics of a stochastically perturbed two-body problem, Proc. R. Soc. A 463 (2080) (2007) 979–1003.

[31] F. Pierret, Stochastic Gauss equations, Celestial Mech. Dynam. Astronom. 124 (2) (2014) 109–126, http://dx.doi.org/10.1007/s10569-015-9652-1, [Online]. Available: http://arxiv.org/abs/1402.1758.

[32] M. Manzi, M. Vasile, Analysis of stochastic nearly-integrable dynamical systems using polynomial chaos expansions, in: 2020 AAS/AIAA Astrodynamics Specialist Conference, South Lake Tahoe, 2020.

[33] M. Vasile, Fast chaos expansions of diffusive and sub-diffusive processes in orbital mechanics, in: 72nd International Astronautical Congress, IAC, 2021.

[34] M. Vasile, M. Manzi, Polynomial stochastic dynamic indicators, Celestial Mech. Dynam. Astronom. (2022) http://dx.doi.org/10.1007/s10569-022-10116-1, Accepted/In press.

[35] F. Olver, D. Lozier, R. Boisvert, C. Clark, NIST HandBook of Mathematical Functions, Cambridge University Press, 2010.

[36] K. Wakker, Fundamentals of Astrodynamics, Institutional Repository Delft University of Technology, Delft, 2015.

[37] A. Wittig, P. Di Lizia, R. Armellin, K. Makino, F. Bernelli-Zazzera, M. Berz, Propagation of large uncertainty sets in orbital dynamics by automatic domain splitting, Celestial Mech. Dynam. Astronom. 122 (3) (2015) 239–261, [Online]. Available: https://link.springer.com/article/10.1007/s10569-015-9618-3.

[38] D. Pérez-Palau, J.J. Masdemont, G. Gómez, Tools to detect structures in dynamical systems using jet transport, Celestial Mech. Dynam. Astronom. 123 (3) (2015) 239–262, [Online]. Available: https://link.springer.com/article/10.1007/s10569-015-9634-3.

[39] A. Capannolo, F. Ferrari, M. Lavagna, Families of bounded orbits near binary asteroid 65803 didymos, J. Guid. Control Dyn. 42 (1) (2019) 189–198, [Online]. Available: https://arc.aiaa.org/doi/10.2514/1.G003437.

[40] D.A. Surovik, D.J. Scheeres, Autonomous maneuver planning at small bodies via mission objective reachability analysis, in: AIAA/AAS Astrodynamics Specialist Conference 2014, American Institute of Aeronautics and Astronautics Inc., 2014, [Online]. Available: https://arc.aiaa.org/doi/abs/10.2514/6.2014-4147.

[41] HERA: Proximity Operations Guidelines Issue 6 Rev 3, European Space Agency, Noordwijk, The Netherlands, Tech. Rep. 2020.

[42] D.J. Scheeres, Orbit mechanics about asteroids and comets, J. Guid. Control Dyn. 35 (3) (2012) 987–997, [Online]. Available: https://arc.aiaa.org/doi/abs/10.2514/1.57247.